bioRxiv preprint doi: https://doi.org/10.1101/2024.11.17.624020; this version posted November 18, 2024. The copyright holder for this preprint (which was not certified by peer review) is the author/funder, who has granted bioRxiv a license to display the preprint in perpetuity. It is made available under aCC-BY-NC 4.0 International license.

Time-Dependent Material Properties and Composition of the Nonhuman Primate Uterine Layers Through Gestation

Daniella M. Fodera[1], Echo Z. Xu[2], Camilo A. Duarte-Cordon[2], Michelle Wyss[3], Shuyang Fang[2], Xiaowei Chen[4], Michelle L. Oyen[5], Ivan Rosado-Mendez[6,7], Timothy Hall[6], Joy Y. Vink[8], Helen Feltovich[9], and Kristin M. Myers[2*]

[1]Department of Biomedical Engineering, Columbia University, New York, NY, USA
[2]Department of Mechanical Engineering, Columbia University, New York, NY, USA
[3]Department of Biomedical Engineering, Virginia Tech, Blacksburg, VA, USA
[4]Department of Pathology and Cell Biology, Columbia University Irving Medical Center, New York, NY, USA
[5]Department of Biomedical Engineering, Wayne State University, Detroit, MI USA
[6]Department of Medical Physics, University of Wisconsin-Madison, Madison, WI, USA
[7]Department of Radiology, University of Wisconsin-Madison, Madison, WI, USA
[8]Department of Obstetrics & Gynecology, John A. Burns School of Medicine, University of Hawai'i at Mānoa, Honolulu, HI, USA
[9]Department of Obstetrics & Gynecology, North Memorial Health System, Robbinsdale, MN, USA
[*]kmm2233@cumc.columbia.edu

ABSTRACT

The uterus is central to the establishment, maintenance, and delivery of a healthy pregnancy. Biomechanics is an important contributor to pregnancy success, and alterations to normal uterine biomechanical functions can contribute to an array of obstetric pathologies. Few studies have characterized the passive mechanical properties of the gravid human uterus, and ethical limitations have largely prevented the investigation of mid-gestation periods. To address this key knowledge gap, this study seeks to characterize the structural, compositional, and time-dependent micro-mechanical properties of the nonhuman primate (NHP) uterine layers in nonpregnancy and at three time-points in pregnancy: early 2nd, early 3rd, and late 3rd trimesters. Distinct material and compositional properties were noted across the different tissue layers, with the endometrium-decidua being the least stiff, most viscous, least diffusible, and most hydrated layer of the NHP uterus. Pregnancy induced notable compositional and structural changes to the endometrium-decidua and myometrium, but no micro-mechanical property changes. Further comparison to published human data revealed notable similarities across species, with minor differences noted for the perimetrium and nonpregnant endometrium. This work provides insights into the material properties of the NHP uterus and demonstrates the validity of NHPs as a model for studying certain aspects of human uterine biomechanics.

KEYWORDS: uterus, pregnancy, nanoindentation, poro-viscoelasticity, reproductive biomechanics

bioRxiv preprint doi: https://doi.org/10.1101/2024.11.17.624020; this version posted November 18, 2024. The copyright holder for this preprint (which was not certified by peer review) is the author/funder, who has granted bioRxiv a license to display the preprint in perpetuity. It is made available under aCC-BY-NC 4.0 International license.

Introduction

The biomechanical functions of the female reproductive system critically underpin the dynamic physiologic processes of pregnancy[1,2]. The uterus, in particular, undergoes dramatic growth and remodeling in pregnancy to enable fetal growth and development[3–6]. Biomechanical defects to this organ, at the cell and tissue length scales, are thought to cause an array of obstetric disorders, including, but not limited to, preterm birth, intrauterine growth restriction, and uterine rupture, which in turn contribute to the high incidence of maternal and fetal morbidity and mortality in the United States[1,7–11]. To elucidate the role of biomechanics in the pathogenesis of obstetric conditions, a baseline knowledge of normal uterine structure, composition, and mechanics throughout the course of pregnancy is first needed.

Anatomically, the human uterus is an inverted, pear-shaped organ with a single uterine cavity[1,3,12]. The uterine wall is composed of three structurally and functionally distinct tissue layers: (i) the endometrium-decidua, (ii) the myometrium, and (iii) the perimetrium (i.e., serosa)[1,3,12]. The endometrium-decidua is the innermost uterine layer that is composed of luminal and glandular epithelial cells, stromal cells, and spiral arteries embedded in a collagen-dense extracellular matrix (ECM)[3,13]. In nonpregnancy, the endometrium undergoes cyclic cellular and molecular changes throughout the menstrual cycle in response to hormonal fluctuations[13]. The decidua, the pregnant counterpart of the endometrium, forms the basis of the maternal-fetal interface, providing critical nutritional support and immunological protection for the developing fetus[3]. The myometrium, the middle and thickest layer of the uterus, is primarily composed of smooth muscle fascicles interwoven with collagen and elastin fibers and pocketed with blood vessels[3]. Throughout pregnancy, the myometrium must undergo passive growth and stretch to accommodate the growing size of the fetus through smooth muscle cell hyperplasia and hypertrophy[3]. In addition to passive mechanical functions, the myometrium exhibits active contractile behavior to enable sperm motility and menstrual blood egress in nonpregnancy and forceful uterine contractions during labor[3]. Exterior to the myometrium and adjacent to the abdominal cavity is the perimetrium, a thin collagen-dense tissue layer that acts as a smooth, lubricated barrier for the uterus[3,12].

The pregnant human uterus is a protected environment, and ethical considerations limit deep structure-function investigations to two distinct physiologic stages: nonpregnancy and late 3rd trimester[1]. To overcome this barrier, animal models have been previously used to interrogate mid-gestational changes to maternal and fetal physiology, however, gross reproductive anatomy and pregnancy characteristics differ dramatically across mammalian species[14–16]. The anatomic and physiologic similarities of Rhesus macaques (*Macaca mulatta*) and humans are well established[17,18]. With regards to the uterus, both species have three distinct uterine layers surrounding a single uterine cavity, undergo menstruation in nonpregnancy, and most often carry singleton pregnancies to term (Fig. 1)[17,18]. Humans and Rhesus macaques notably differ in total gestational length (270 vs 160 days), depth of embryo implantation, degree of decidualization during the menstrual cycle, number of placental discs, overall lifespan (30 vs 70 yrs), and method of locomotion (bipedal vs quadrupedal)[3,17,18].

Previous work has characterized the passive material properties of the human uterus at multiple length scales, yet no studies to date have evaluated the mechanics of the NHP uterus[19–27]. On the nanometer to micrometer length scale, nanoindentation has been previously employed by our group to measure the time-dependent material properties of all three uterine layers for

bioRxiv preprint doi: https://doi.org/10.1101/2024.11.17.624020; this version posted November 18, 2024. The copyright holder for this preprint (which was not certified by peer review) is the author/funder, who has granted bioRxiv a license to display the preprint in perpetuity. It is made available under aCC-BY-NC 4.0 International license.

humans in nonpregnancy and late 3rd trimester[20]. Significant variations in all material properties were noted across tissue layers, with the endometrium-decidua being the least stiff, most viscous, and least permeable layer[20]. In human pregnancy, the endometrium-decidua layer exhibited increases in stiffness, viscoelastic ratio, and diffusivity, while no changes were observed for the myometrium or perimetrium[20]. Further, a study by Abbas et al. (2019) measured the stiffness of nonpregnant endometrium and first-trimester decidua tissues with atomic force microscopy and noted no change in stiffness between these tissue types at the micro-scale[19]. For larger testing regimes on the millimeter to centimeter length scale, studies have exclusively characterized the myometrium in nonpregnancy and late pregnancy using tension, compression, indentation, and shear[21–27]. Overall, the human myometrium exhibits nonlinearity, anisotropy, and tension-compression asymmetry, with nonpregnant tissue exhibiting increased stiffness and decreased extensibility compared to pregnant tissue[21–27].

It is presently unknown how the material and structural properties of the human uterus change in a healthy pregnancy between the first and third trimesters. Therefore, we seek to utilize a nonhuman primate (NHP) model to characterize mid-gestational changes to the mechanical and structural properties of the uterus, distinguishing across all three tissue layers (Fig. 1). Specifically, this study will investigate nonpregnant (NP) and pregnant (PG) states in early 2nd (E2), early 3rd (E3), and late 3rd (L3) trimesters. We expect that mechanical and structural changes observed in the NHP model will mimic trends noted previously for humans and enable a more complete biomechanical understanding of pregnancy.

Results

Structure and Composition of NHP Uterine Layers

The structure and composition of all three uterine tissue layers (i.e., endometrium-decidua, myometrium, and perimetrium) were evaluated from NHP subjects (i.e., Rhesus macaques) in nonpregnancy (N = 3) and pregnancy at E2 (N = 3), E3 (N = 3), and L3 (N = 5) trimesters (Fig. 1). All tissues were reviewed by a board-certified pathologist and appeared largely normal for the cohort of NHPs investigated in this study (Fig. 2A). The uterine tissue layers of the NHP exhibited distinct structure and composition of ECM and cellular components. In nonpregnancy, the endometrium was primarily composed of pseudo-stratified epithelial glands and densely-packed stromal cells with a small proportion of immune cells. Blood vessels comprised less than 10% of the overall endometrial tissue area and were concentrated in the basalis layer immediately adjacent to the myometrium (Fig. 2E). Collagen was diffusely present in the stromal spaces of the endometrium and tightly surrounded the endometrial glands to act as a basement membrane (Fig. 2A). Compared to the superficial functionalis layer of the endometrium, increased deposition of collagen was found in the basalis layer. Variations in the menstrual cycle stage were observed for each NP subject, which is noted in Table S1.

In pregnancy, the endometrium dramatically remodels into the decidua. All decidua tissue taken from NHPs in this study can be classified as decidua parietalis, distant from the sites of placentation. Overall, the epithelial glands appeared flattened, and decidualized stromal cells adopted a polygonal shape (Fig. 2A). Blood vessels continued to be present in the PG decidua, both superficially and deep, but displayed no notable changes in size and concentration relative to nonpregnancy (Fig. 2E).

bioRxiv preprint doi: https://doi.org/10.1101/2024.11.17.624020; this version posted November 18, 2024. The copyright holder for this preprint (which was not certified by peer review) is the author/funder, who has granted bioRxiv a license to display the preprint in perpetuity. It is made available under aCC-BY-NC 4.0 International license.

Collagen was diffusely present throughout the decidua tissue and was concentrated around blood vessels (Fig. 2A). No notable changes to the structure and composition of the decidua were observed across E2, E3, and L3 gestational groups (Fig. 2A).

The myometrium, the middle and thickest layer of the uterus, exhibited longitudinal alignment of smooth muscle fibers surrounded by thick bands of collagen for all NHP subjects (Fig. 2A). Blood vessels represented, on average, 10% or less of the overall myometrial tissue area; the largest blood vessels appeared centered in the middle third of the uterine wall (Fig. 2E). In pregnancy, the smooth muscle cells of the myometrium underwent hypertrophy, exhibiting an increase in cell volume. The relative proportion of smooth muscle to collagen content increased in late third trimester relative to nonpregnancy as determined through semi-quantitative image analysis (Fig. 2C). No change in the distribution and size of blood vessels was noted for the myometrium in pregnancy (Fig. 2E). Interestingly, a unique phenomenon of focal edema was observed for all L3 pregnant tissues evaluated: increased interstitial spacing between the collagen and smooth muscle cells (Fig. 2B). This histological feature was not observed for either E2 or E3 groups and given its localized nature and consistency of appearance for all L3 tissues, it is unlikely to be the product of a histological artefact.

Lastly, the perimetrium, also known as the serosa, appeared as a thin, smooth band of collagen adjacent to the myometrium (Fig. 2A). In a subset of samples, thicker regions of collagen indicative of fibrosis and small amounts of vasculature were visible in the perimetrium (Table S1). No overt changes to this tissue layer as a result of pregnancy were noted (Fig. 2A).

In addition to histological analysis, the hydration of each uterine layer was quantified by means of lyophilization. Tissue hydration was determined to be distinct across uterine tissue layers (endometrium-decidua: $83.2 \pm 2.7\%$; myometrium: $80.2 \pm 1.4\%$; perimetrium: $74.3 \pm 3.5\%$), with the perimetrium the least hydrated tissue layer of the uterus (Fig. 2D). No change in hydration was observed across gestation for any uterine tissue layer (Fig. 2D).

Material Properties of NHP Uterine Layers

Spherical nanoindentation ($R = 50\ \mu$m) was employed in this study to measure the time-dependent material properties of NHP uterine layers, namely the endometrium-decidua, myometrium, and perimetrium, across gestation (Fig. 3A). Tissues were taken from three anatomic regions (i.e., anterior, fundus, and posterior) from the same NP, E2, E3, and L3 animal subjects described previously (Fig. 1). Approximately 100 indentation points were measured for each tissue sample, representing more than 12,000 individual indentation measurements in all. To describe the uterus' intrinsic viscoelasticity (rearrangement of the solid matrix) and poroelasticity (fluid flow migration), phenomena known to be exhibited by soft biological tissues[28–30], an established poroelastic-viscoelastic (PVE) constitutive model[31] was employed to determine the following material parameters: instantaneous elastic modulus (E_0), equilibrium elastic modulus (E_∞), poroelastic modulus (E_{PE}), viscoelastic ratio (E_∞/E_0), intrinsic permeability (k), and diffusivity (D). Representative force versus indentation depth and force versus time curves are shown in Figs. 3B and C.

Surprisingly, no changes in any of the material parameters were observed across gestation for the endometrium-decidua, myometrium, and perimetrium tissue layers (Fig. 3E, Fig. 4B,D,F). The greatest differences in material properties were found across uterine layers for each gestational group evaluated (Fig. 3D). All elastic modulus parameters (E_0, E_∞, and E_{PE}),

bioRxiv preprint doi: https://doi.org/10.1101/2024.11.17.624020; this version posted November 18, 2024. The copyright holder for this preprint (which was not certified by peer review) is the author/funder, who has granted bioRxiv a license to display the preprint in perpetuity. It is made available under aCC-BY-NC 4.0 International license.

which are measures of tissue stiffness (resistance to deformation), ranged from 10^1 to 10^4 Pa, were highly correlated with one another, and exhibited identical trends across tissue layers and gestational groups. Overall, tissue stiffness increased from the intra-uterine cavity to the outer abdominal cavity, with the endometrium-decidua being the least stiff and the perimetrium being the most stiff (Fig. 3D). The perimetrium was stiffer than the endometrium-decidua for all gestational groups evaluated; only for PG time points was the perimetrium stiffer than the myometrium (Fig. 3D). Spatial variations in tissue stiffness (E_r) were assessed across the entire uterine wall thickness(Fig. 3F). Notably, a stiffness gradient at the interface between the endometrium-decidua and myometrium tissue layers was captured (Fig. 3F). Across the individual elastic modulus paramters measured, instantaneous elastic modulus (E_0), as expected, was greater than the equilibrium elastic modulus (E_∞) for all samples (Fig. 3G). Between E_∞ and E_{PE}, no difference was observed for the myometrium and perimetrium tissue layers, but there was a minute but systemic increase in E_{PE} relative to E_∞ for the endometrium-decidua layer for all gestational groups (Fig. 3G).

Median values of viscoelastic ratio (E_∞/E_0) ranged between 0.3 and 0.6 for all samples evaluated, indicating that the uterus possesses both solid-like and fluid-like material behavior (Fig. 4A,B). The endometrium-decidua layer was determined to be slightly more viscous (0.43 ± 0.05) than the myometrium (0.50 ± 0.04) and perimetrium (0.49 ± 0.04) layers for all gestational groups (Fig. 4A). No statistically significant difference in viscoelastic ratio was observed between the myometrium and perimetrium layers except in the L3 group (Fig. 4A). Intrinsic permeability (k) is an innate property of a porous medium (e.g., biological tissue) that describes a material's resistance to fluid flow as a product of its pore geometry. Values of intrinsic uterine permeability ranged between 10^1 to 10^3 nm^2 for all tissue layers (Fig. 4C,D). For all gestational groups, the permeability of the perimetrium (87 ± 68 nm^2) was slightly less than the endometrium-decidua (110 ± 53 nm^2) and myometrium (131 ± 70 nm^2) layers (Fig. 4C). Slight variations in permeability values between the endometrium-decidua and myometrium layers occurred only for E3 and L3 groups (Fig. 4C). At this length scale of material testing, average pore size (ξ), whereby $\xi \sim \sqrt{k}$, was determined to be in the range of 4 to 14 nm. Lastly, diffusivity (D), also known as the diffusion coefficient, is a measure that describes the flow of fluid through a porous medium over time. For the uterus, diffusivity is significantly decreased in the endometrium-decidua layer, by more than an order of magnitude ($0.45 \pm 1.07\ x\ 10^{-10}\ m^2/s$), when compared to the myometrium ($4.79 \pm 2.43\ x\ 10^{-10}\ m^2/s$) and perimetrium ($4.82 \pm 1.13\ x\ 10^{-10}\ m^2/s$) layers (Fig. 4).

The effect of tissue and subject characteristics on the material properties of the uterus was also investigated in this study. Across the three anatomic regions evaluated (i.e., anterior, posterior, and fundus), regional variations in all material properties occurred on an individual animal basis for each of the tissue layers and gestational groups but such differences were not systemic when data from all NHP subjects were considered (Fig. S2). Further, no material properties reported in this study correlated linearly with animal age and gravidity, defined as the total number of previous pregnancies (Fig. S3). To note, age and gravidity were considered together in the linear regression model since, in this cohort of NHPs studied, there was an increasing linear correlation between animal age and gravidity (Fig. S1).

Further investigation into the inter-correlation of material properties revealed a unique scattering of data between tissue

bioRxiv preprint doi: https://doi.org/10.1101/2024.11.17.624020; this version posted November 18, 2024. The copyright holder for this preprint (which was not certified by peer review) is the author/funder, who has granted bioRxiv a license to display the preprint in perpetuity. It is made available under aCC-BY-NC 4.0 International license.

stiffness and permeability, which was characteristic of each distinct uterine tissue layer (Fig. 5B). Notably, the perimetrium exhibits one primary cluster of data with a negative linear relationship between stiffness and permeability, while the myometrium displays two distinct, linearly aligned data clusters (Fig. 5A). No relationship between permeability and stiffness exists for the endometrium-decidua tissue layer (Fig. 5).

Comparative Analysis of Human and Rhesus Macaque Uterine Layer Material Properties

Nanoindentation data generated by this study on NHP uterine layers was directly compared to published data for the human uterus that employed similar methodologies[19,20]. Notable similarities and differences in the time-dependent material properties of the human and NHP uterus were found in nonpregnancy and late third trimester (Fig. 6). Comparing between humans and NHPs, no significant differences in the values of viscoelastic ratio, permeability, and diffusivity were found for all three uterine tissue layers for NP and L3 PG time points (Fig. 6). Interestingly, the relative changes between NP and PG groups are notably different for the endometrium-decidua tissue layer. In humans, there is a statistically significant increase in the viscoelastic ratio, permeability, and diffusivity parameters for the PG decidua relative to the NP endometrium[20]. Such trends are absent for NHPs.

The elastic moduli of the endometrium-decidua and perimetrium tissue layers were found to be the most different between humans and NHPs; no species-related differences in myometrium stiffness were detected (Fig. 6). In particular, the NP endometrium is significantly less stiff in humans compared to NHPs and undergoes stiffening in human pregnancy in a rather linear fashion (Fig. 6). Additionally, for all gestational groups evaluated, the perimetrium of humans is significantly less stiff than that of NHPs (Fig. 6). Further, it is important to note that a greater degree of variation in elastic modulus is observed in NHPs layers compared to humans, as evidenced by larger standard deviation values (Fig. 6).

Discussion

Here, we evaluate the structure-function relationship of the NHP uterus from nonpregnancy to late pregnancy, investigating differences across tissue layers and mid-gestational time points. Specifically, this nanoindentation dataset, together with histological and biochemical analysis, highlights drastic differences in structure, composition, and time-dependent material properties across the endometrium-decidua, myometrium, and perimetrium tissue layers. Interestingly, although pregnancy induces clear structural and compositional changes to the uterus, particularly for the endometrium-decidua and myometrium layers, such differences are not reflected by alterations to uterine material properties on the microscale.

This robust nanoindentation dataset contributes to a key knowledge gap in pregnancy biomechanics given the insurmountable ethical boundaries associated with human pregnancy. Similar to trends previously reported for human uterine tissue, NHP pregnancy brought about no differences in the values of stiffness, viscoelastic ratio, permeability, or diffusivity for the myometrium and perimetrium. A significant difference in the baseline stiffness of the NP endometrium and perimetrium was noted between the two species, with NHP tissue being slightly stiffer. Yet, these disparities in stiffness values are still within the same order of magnitude and may reflect a slight sampling bias in the human dataset. Notably, the human dataset exclusively evaluates the anterior region of the uterus, whereas the NHP dataset represents a greater sampling of anatomic

bioRxiv preprint doi: https://doi.org/10.1101/2024.11.17.624020; this version posted November 18, 2024. The copyright holder for this preprint (which was not certified by peer review) is the author/funder, who has granted bioRxiv a license to display the preprint in perpetuity. It is made available under aCC-BY-NC 4.0 International license.

regions, including the anterior, posterior, and fundus. Such differences in sampling approaches are likely responsible for the greater variability in NHP material properties measured. Further, a small number of subjects (n = 3–6 per gestational group) are characterized in both the human and NHP datasets, and confounding variables such as age, menstrual cycle stage, gravidity, and gynecologic disorders are not fully represented. Still, remarkable similarities in the material, structural, and compositional properties are noted between the two species, thereby suggesting that NHPs are a valid model for studying certain aspects of human uterine biomechanics in healthy and diseased states, particularly those affecting the myometrium. It is well-documented that several gynecologic and obstetric pathologies are shared between NHPs and humans, namely endometriosis, adenomyosis, leiomyoma, prolapse, cancer, ectopic pregnancies, pre-eclampsia, premature delivery, and stillbirth[32–35]. The potential role mechanics plays in the pathogenesis of these disorders has yet to be fully elucidated in humans, and therefore, NHPs may serve as a valuable model for investigation.

The absence of material property changes observed across gestation for each of the tissue layers may either reflect a true intrinsic lack of differences induced by pregnancy in NHPs or may be a product of the length scale and microstructural engagement associated with nanoindentation testing. Under indentation, samples are subjected to a complex loading profile of compression, radial tension and shear[36]. Comparing with data previously reported for the human myometrium, the stiffness of the myometrium was not altered in third-trimester pregnancy under indentation across nanometer to millimeter lengths scales up to 45% strain[20–22]. Only under tensile loads for strains above 30% was the extensibility of the myometrium increased relative to nonpregnancy[22]. Therefore, softening of the pregnant NHP uterus may still occur at mid-gestation time points, but different mechanical testing approaches may be needed to elucidate such trends. Further, this asymmetry in mechanical behavior under modalities of indentation and tension highlights fundamental differences in the contribution of the fiber network and ground substance to the overall material behavior of this tissue[22,37]. Under compression, the mechanical response of a biological tissue is largely dictated by the properties of its nonfibrillar ground substance, which is provided, in large part, by the glycosaminoglycans (GAGs), proteoglycans, and fluid[37,38]. The fiber network alone cannot sustain compression but does constrain the lateral expansion of the ground matrix[38]. Engagement of the fiber network primarily occurs under tension through fiber uncrimping, alignment, and sliding[37–39]. Therefore, since only tensile testing at large strains reveals softening of the human myometrium in late pregnancy, collagen fiber engagement is necessary for observing this material behavior in pregnancy. Given the overlap in material properties for the human and NHP myometrium noted in this study, we posit that the NHP will exhibit similar tension-compression asymmetry and softening under tension in the large-strain regime. Unfortunately, no mechanical data outside the nanoscale and low-strain regime exists for the endometrium and perimetrium tissue layers, and it is impossible to predict whether similar trends are observed when such tissues are subjected to different mechanical loading profiles at larger length scales[19,20].

It is evident from the data presented in this study that the time-dependent material properties vary across the three uterine layers which are structurally and functionally distinct. Intrinsic viscoelasticity and poroelasicity are two distinct yet overlapping mechanisms contributing to the time-dependent behavior of the uterus, describing the conformational rearrangement of macro-

bioRxiv preprint doi: https://doi.org/10.1101/2024.11.17.624020; this version posted November 18, 2024. The copyright holder for this preprint (which was not certified by peer review) is the author/funder, who has granted bioRxiv a license to display the preprint in perpetuity. It is made available under aCC-BY-NC 4.0 International license.

molecules and displacement-induced fluid redistribution, respectively[38,40]. In hydrogels, it is well understood that the dominant relaxation mechanism depends largely on whether the material is polymerized through physical (non-covalent) or chemical (covalent) cross-linking; viscoelastic behavior dominates in physically cross-linked hydrogels, while poroelastic relaxation dominates in chemically cross-linked gels[41,42]. Biological tissues, however, exhibit greater structural and compositional complexity compared to hydrogels which are largely homogeneous, and their time-dependent behaviors cannot be as simply described. The identity (e.g., collagen, elastin, proteoglycans) and organization (e.g., cross-linking, fiber alignment, pore size) of a tissue's ECM and cellular components can contribute to alterations in the energy dissipation profiles, however the role of each of these components in influencing a tissue's time-dependent material behavior has yet to be fully elucidated[43–45]. In this study, the combined effect of poroelasticity and viscoelasticity was considered with the utilization of the PVE model, however, it is important to note that this model employs an analytical, semi-phenomenologic fit of the load relaxation data and extrinsic experimental parameters such as ramp time, indentation depth, and probe radius can modulate the measured time-dependent material behavior of the tissues[40,41,46]. Therefore, further investigation is needed to elucidate the relative contributions of poroelastic and viscoelastic mechanisms of the distinct uterine layers across multiple length and time scales.

Additionally, it is interesting to consider the relationship between the time-dependent material properties measured in this study, notably elastic modulus and intrinsic permeability. We posit that the distinct clustering of the data points on the elastic modulus versus permeability plots is indicative of the heterogeneous composition of cellular and ECM components intrinsic to each of the tissue layers and therefore, represents a unique, biophysical fingerprint for each of the tissue layers. However, due to inherent limitations to the methods outlined in this study, individual ECM and cellular components contributing to said spatial heterogeneity cannot be identified. Additional experiments on isolated components are needed to elucidate the physical meaning of this relationship.

It is important to consider that the results generated in this study represent a particular length scale (nanometer to micrometer) of tissue material properties and do not capture the full multiscale properties of these tissues. Namely, permeability, and by extension, pore size, measurements reported in this study are biased towards smaller values due to the physical limits of nanoindentation testing and, therefore, do not capture the larger interconnected pore network likely present in these tissues[47]. Unfortunately, no studies to date have directly measured the permeability of the uterus *a priori*. Measurements conducted on the human cervix tissue with a passive pressure gradient reported values of permeability several orders of magnitude greater than that which is reported for the NHP and human uterus[20,48]. Additionally, when compared to other biological tissues characterized by nanoindentation, permeability values of the uterus appear greater than cartilage or heart tissue but less than the liver or kidney, thereby highlighting the relative importance of fluid transport in the uterus[31,47].

On a structural and compositional basis, the greatest differences are observed across the three uterine tissue layers regardless of PG state; only the endometrium-decidua and myometrium tissue layers exhibit notable changes as a result of pregnancy. Specifically, the L3 myometrium displays a shift in the relative proportion of smooth muscle and collagen components within a mm^2 tissue area, which is accompanied by the histological feature of focal edema. The increased interstitial spacing of the

bioRxiv preprint doi: https://doi.org/10.1101/2024.11.17.624020; this version posted November 18, 2024. The copyright holder for this preprint (which was not certified by peer review) is the author/funder, who has granted bioRxiv a license to display the preprint in perpetuity. It is made available under aCC-BY-NC 4.0 International license.

tissue's microstructure is indicative of increased swelling of the myometrium in the late third trimester of pregnancy. Such changes in fluid homeostasis may be a result of microvascular pressure shifts or changes in the composition of hydrophilic ECM proteins (e.g., proteoglycans and hyaluronan)[49,50]. Interestingly, this phenomenon is not reflected by quantitative tissue hydration measurements reported in this study which show no change in the overall hydration of the myometrium with pregnancy.

Overall, this study establishes the normal heterogeneity of material, structural, and compositional properties across the NHP uterine layers in nonpregnant and pregnant states, revealing notable similarities to the human uterus. Characterizing baseline changes that occur throughout healthy pregnancies in a physiologically comparable NHP animal model is foundational to better understanding and predicting healthy and disordered alterations in human gestation with *in vitro*, *in vivo*, and *in silico* research approaches.

Methods

Tissue Collection

Following approval by the University of Wisconsin Institutional Animal Care and Use Committee (IACUC), NHP uterine tissue was collected from nonpregnant (N = 3) and pregnant Rhesus macaques following total hysterectomies. PG uterine tissue was collected at three gestational time points corresponding approximately to the early 2^{nd} (E2, N = 3), early 3^{rd} (E3, N = 3), and late 3^{rd} (L3, N = 5) trimesters (Fig. 1). Detailed animal subject information including age, gestational age, gravidity, placenta location and past obstetric history are noted in Table 1. Uterine specimens contained all three tissue layers (i.e., endometrium-decidua, myometrium, and perimetrium) and were sampled from three anatomic regions: anterior, fundus, and posterior. Samples were flash-frozen on dry ice and stored at -80ºC until testing.

Histology

For each NHP subject, uterine cross-sections, which contained all three tissue layers, were prepared for histology; only one anatomic region per subject was included. Samples were fixed in 10% formalin solution for 24 hrs and subsequently transferred to 70% ethanol solution. Samples were paraffin-embedded and sectioned to a thickness of 5 µm by the Molecular Pathology Core Facilities at Columbia University Irving Medical Center (CUIMC). To observe histomorphology, all samples were stained for Hemotoxylin & Eosin (H&E) and Masson's Trichrome using standard protocols[51]. Samples were imaged under brightfield microscopy with a Leica Aperio AT2 whole slide scanner up to 20x magnification and visualized with the Aperio ImageScope software (v12.3.1.6002, Leica Microsystems, Wetzler, Germany). All slides were reviewed by a board-certified pathologist (X.C.) who specializes in gynecologic pathology and cytopathology.

Image Quantification

The relative proportions of collagen and smooth muscle content in the myometrium were quantified from Masson's Trichrome stained tissue. Three representative images per NHP subject were taken at 10x magnification with a Leica DMi1 Inverted

bioRxiv preprint doi: https://doi.org/10.1101/2024.11.17.624020; this version posted November 18, 2024. The copyright holder for this preprint (which was not certified by peer review) is the author/funder, who has granted bioRxiv a license to display the preprint in perpetuity. It is made available under aCC-BY-NC 4.0 International license.

Microscope using the Leica Application Suite X (LAS-X). For this quantification, regions containing blood vessels in more than fifty percent of the image area were avoided. The areas of blue and red color, corresponding to collagen and smooth muscle content, respectively, were quantified in ImageJ (NIH, Bethesda, MD, USA) with RGB color deconvolution and a thresholding function.

Additional analysis was conducted to quantify the number and size of blood vessels in the endometrium-decidua and myometrium tissue layers for each animal subject. Blood vessels were manually identified on Masson's Trichrome stained uterine cross sections using Aperio ImageScope's annotation tool. The areas (μm^2) of each blood vessel and tissue layer region were recorded.

Tissue Hydration

Lyophilization was used to determine tissue hydration of all NHP uterine layers using a FreeZone 4.5 Liter Benchtop Freeze Dry System (Labconco, Kansas City, MO). For each tissue layer, three tissue samples per animal subject were analyzed. All samples were taken from the posterior region of the uterus and dissected into small (mm^3) pieces. Wet and dry sample weights were measured in a pre-weighed 1.5 ml Eppendorf tube before and after lyophilization using an analytical balance (MS105, Mettler Toledo, Greifensee, Switzerland) with 0.01 mg readability. Tissue hydration was calculated with the following equation:

$$Hydration = \frac{\textit{Wet weight - Dry weight}}{\textit{Wet weight}} x100 \tag{1}$$

Nanoindentation Testing

Spherical nanoindentation (Piuma, Optics11Life, Amsterdam, NE) was utilized to determine the material properties of uterine tissue. A 50 μm probe radius with a cantilever stiffness of 0.15 – 0.5 N/m was used. In preparation for testing, samples were dissected, adhered to a glass dish with superglue (Krazy Glue, Atlanta, GA), and swelled at 4°C overnight in 1X PBS solution supplemented with 2 mM ethylenediaminetetraacetic acid (EDTA). Immediately prior to testing, the sample was equilibrated to room temperature for 30 minutes and subsequently tested in Opti-free contact lens solution (Alcon, Fort Worth, TX, USA) to reduce adhesion between the glass probe and sample[52]. Tissues were indented to a fixed depth of 4 μm under indentation control, corresponding to a 5% indentation strain and contact area of 380 μm^2. Following a 2 s ramp to the prescribed indentation depth, the probe's position was held for 15 s to yield a load relaxation curve approaching equilibrium. All tissue sections were at least 1 mm thick and tested within two freeze-thaw cycles.

Individual Uterine Tissue Layers

The material properties of individual uterine tissue layers were measured at three anatomic regions (i.e., anterior, fundus, and posterior) for all gestational groups. To ensure reliable measurements taken for thinner tissue layers, the surface of the endometrium-decidua, and perimetrium were directly tested. The orientation of the myometrium was variable and not explicitly noted. Given that the size and geometry of the tissues were so irregular, the number of indentation points also

bioRxiv preprint doi: https://doi.org/10.1101/2024.11.17.624020; this version posted November 18, 2024. The copyright holder for this preprint (which was not certified by peer review) is the author/funder, who has granted bioRxiv a license to display the preprint in perpetuity. It is made available under aCC-BY-NC 4.0 International license.

varied; approximately 100 points were measured per sample to capture sufficient intra-sample variability. The distance between individual indentations was kept constant at 200 μm.

Uterine Wall Cross Sections

Spatial stiffness variations were assessed across the entire length of the posterior uterine wall tissue section from the perimetrium to the endometrium-decidua. One subject per gestational group was assessed. The width of the tested region was kept constant at 1mm and the distance between individual indentations was fixed at 200 μm.

Nanoindentation Data Analysis

Poroelastic-Viscoelastic (PVE) Model

For individual tissue layers, load versus time data from the hold portion of the indentation protocol were fit with a combined poroelastic-viscoelastic (PVE) model in Matlab based on an established analytical solution with a nonlinear least-squares solver[40,41,53]. The coupled effect of the material's poroelastic (P_{PE}) and viscoelastic (P_{VE}) force responses is described by:

$$P_{PVE}(t) = \frac{P_{PE}(t) \cdot P_{VE}(t)}{P_\infty} \tag{2}$$

The viscoelastic force response is calculated using a generalized Maxwell model, consisting of a linear spring connected in parallel with two Maxwell units, each containing a linear spring and dashpot connected in series. The viscoelastic component of the model is defined by the following equation:

$$P_{VE}(t) = \frac{16 \cdot h^{3/2} \cdot R^{1/2}}{9} \cdot [E_s + \sum_n E_n \cdot X_n \cdot exp(-t/\tau_n)] \tag{3}$$

where E_s and E_n are the elastic moduli of the linear spring and the n^{th} Maxwell element (n = 2), respectively, h is the applied indentation depth, R is the probe radius, and τ_n is the characteristic relaxation time of the n^{th} Maxwell element (n = 2). A ramp correction factor ($X_n = (\tau_n/t_r) \cdot [exp(-t_r/\tau_n) - 1]$) is included to account for the two-second ramp time (t_r) since the original Maxwell model assumes a step loading function[54]. Instantaneous elastic modulus (E_0) and equilibrium elastic modulus (E_∞) parameters are determined from Eqn. 3 when $t = 0$ and $t = \infty$, respectively.

The poroelastic force response is calculated from the analytical solution published in Hu et al. 2010:

$$P_{PE}(t) = P_\infty + (P_0 - P_\infty) \cdot [0.491 \cdot exp(-0.908 \cdot \sqrt{t/\tau_p} + 0.509 \cdot exp(-1.679 \cdot (t/\tau_p)] \tag{4}$$

P_0 is the initial force at the beginning of the load relaxation curve and is calculated from the model defined in Hu et al. 2010 as $P_0 = (16/3) \cdot G_{PE} \cdot R^{1/2} \cdot \delta_0{}^{3/2}$, where G_{PE} is the apparent poroelastic shear modulus. P_∞ is the estimated equilibrium force given by $P_\infty = P_0/[2(1-\nu_d)]$, where ν_d is the drained Poisson's ratio. τ_p is the poroelastic time constant in the defined as $\tau_p = a^2/D$, where a is the indentation contact radius ($a = \sqrt{R \cdot h}$) and D is diffusivity. Intrinsic permeability (k) is calculated as

bioRxiv preprint doi: https://doi.org/10.1101/2024.11.17.624020; this version posted November 18, 2024. The copyright holder for this preprint (which was not certified by peer review) is the author/funder, who has granted bioRxiv a license to display the preprint in perpetuity. It is made available under aCC-BY-NC 4.0 International license.

follows:

$$k = \frac{D\mu(1-2\nu_d)}{2G_{PE}(1-\nu_d)} \quad (5)$$

The interstitial fluid viscosity (μ) is assumed to be equivalent to the dynamic viscosity of water at 25°C ($\mu = 0.89$ x $10^{-3} Pa \cdot s$). Material incompressibility is assumed, wherein material volume does not change under applied deformation, and therefore, undrained Poisson's ratio (ν) is set as 0.5. The apparent poroelastic modulus (E_{PE}) is calculated from apparent poroelastic shear modulus as $E_{PE} = 3G_{PE}$.

Fitted data points were excluded from the final data set if the load relaxation curve displayed (i) sharp discontinuities, (ii) increasing loads over time, or (iii) ΔP $\sim$ ($P_{max} - P_{min}$) less than 0.005 μN.

Hertzian Contact Model

Data for uterine wall cross-sections were analyzed with the Hertzian contact model to reduce the number of points removed due to exclusion criteria. The apparent elastic modulus (E_r) was determined by fitting each load versus indentation curve from the initial loading portion of the indentation protocol with the following equation[31,55]:

$$F = \frac{4 \cdot E_r \cdot R^{1/2} \cdot h^{3/2}}{3 \cdot (1-\nu^2)} \quad (6)$$

where F is the applied force, R is the probe radius, h is the applied indentation depth, and ν is Poisson's ratio. A value of 0.5 is prescribed for ν to align with incompressibility assumptions. This model assumes contact between a sphere and a half-space for a material that is linear elastic. Data fitting was performed with a customized code in Matlab (Mathworks, Natick, MA, USA) using a nonlinear least-squares solver, identical to what has been previously published in the literature[20,41]. Data points were excluded if the corresponding R^2 value was less than 0.5, indicating a poor model fit.

Statistical Analysis

Statistical analysis was performed using RStudio (v1.3.1056) or GraphPad Prism (v.10.0.2) . Normality of all data was first assessed with Q-Q plots. In instances of non-normal data distributions, data were normalized with a logarithmic transformation. A linear mixed-effects model was employed to analyze all datasets in this study which investigated differences across tissue layers or gestational groups. In all cases, animal ID was set as the random variable. Multiple comparisons were assessed with a Tukey post-hoc test. To assess differences in material properties between NHPs and humans[19,20], an unpaired t-test with a Welch correction was performed for each parameter at NP and L3 time points. To determine the inter-correlation of material properties by tissue layer, Pearson correlation coefficients were calculated. Linear regression analysis was performed in noted cases of continuous variables; the multiple R^2 and p values are reported for each fit. Significance was set at a 95% confidence level for all analyses. P-value symbols are defined as follows: $^{\#}p \leq 0.1$, $^{*}p \leq 0.05$, $^{**}p \leq 0.01$, $^{***}p \leq 0.001$, $^{****}p \leq 0.0001$.

bioRxiv preprint doi: https://doi.org/10.1101/2024.11.17.624020; this version posted November 18, 2024. The copyright holder for this preprint (which was not certified by peer review) is the author/funder, who has granted bioRxiv a license to display the preprint in perpetuity. It is made available under aCC-BY-NC 4.0 International license.

References

1. Myers, K. M. & Elad, D. Biomechanics of the human uterus. *WIREs Syst. Biol. Medicine* **9**, e1388, DOI: 10.1002/wsbm.1388 (2017).

2. Myers, K. M. *et al.* The mechanical role of the cervix in pregnancy. *J. Biomech.* **48**, 1511–1523, DOI: 10.1016/j.jbiomech.2015.02.065 (2015).

3. Cunningham, F. G. *et al.* *Williams Obstetrics, 26e* (McGraw Hill, New York, NY, 2022).

4. Woessner, J. F. & Brewer, T. H. Formation and breakdown of collagen and elastin in the human uterus during pregnancy and post-partum involution. *Biochem. J.* **89**, 75–82 (1963).

5. Louwagie, E. M. *et al.* Longitudinal ultrasonic dimensions and parametric solid models of the gravid uterus and cervix. *PLOS ONE* **16**, e0242118, DOI: 10.1371/journal.pone.0242118 (2021).

6. Louwagie, E. M. *et al.* Uterus and cervix anatomical changes and cervix stiffness evolution throughout pregnancy, DOI: 10.1101/2024.05.01.592023 (2024).

7. Scott, A. K., Louwagie, E. M., Myers, K. M. & Oyen, M. L. Biomechanical Modeling of Cesarean Section Scars and Scar Defects. In Skalli, W., Laporte, S. & Benoit, A. (eds.) *Computer Methods in Biomechanics and Biomedical Engineering II*, 67–76, DOI: 10.1007/978-3-031-55315-8_8 (Springer Nature Switzerland, Cham, 2024).

8. Manuck, T. A. *et al.* Preterm Neonatal Morbidity and Mortality by Gestational Age: A Contemporary Cohort. *Am. journal obstetrics gynecology* **215**, 103.e1–103.e14, DOI: 10.1016/j.ajog.2016.01.004 (2016).

9. Hoyert, D. Maternal Mortality Rates in the United States, 2020. Tech. Rep., National Center for Health Statistics (U.S.) (2022). DOI: 10.15620/cdc:113967.

10. Gregory, E., Valenzuela, C. & Martin, J. Fetal Mortality in the United States: Trends From 2014 Through 2019 and Changes Between 2018–2019 and 2019–2020. Tech. Rep., National Center for Health Statistics (U.S.) (2022). DOI: 10.15620/cdc:113008.

11. Fink, D. A. *et al.* Trends in Maternal Mortality and Severe Maternal Morbidity During Delivery-Related Hospitalizations in the United States, 2008 to 2021. *JAMA Netw. Open* **6**, e2317641, DOI: 10.1001/jamanetworkopen.2023.17641 (2023).

12. Ameer, M. A., Fagan, S. E., Sosa-Stanley, J. N. & Peterson, D. C. Anatomy, Abdomen and Pelvis: Uterus. In *StatPearls* (StatPearls Publishing, Treasure Island (FL), 2023).

13. Critchley, H. O. D., Maybin, J. A., Armstrong, G. M. & Williams, A. R. W. Physiology of the Endometrium and Regulation of Menstruation. *Physiol. Rev.* **100**, 1149–1179, DOI: 10.1152/physrev.00031.2019 (2020).

14. Elovitz, M. A. & Mrinalini, C. Animal models of preterm birth. *Trends Endocrinol. & Metab.* **15**, 479–487, DOI: 10.1016/j.tem.2004.10.009 (2004).

bioRxiv preprint doi: https://doi.org/10.1101/2024.11.17.624020; this version posted November 18, 2024. The copyright holder for this preprint (which was not certified by peer review) is the author/funder, who has granted bioRxiv a license to display the preprint in perpetuity. It is made available under aCC-BY-NC 4.0 International license.

15. Andersen, M. D. *et al.* Animal Models of Fetal Medicine and Obstetrics. In *Experimental Animal Models of Human Diseases - An Effective Therapeutic Strategy*, DOI: 10.5772/intechopen.74038 (IntechOpen, 2018).

16. Machado, D. A., Ontiveros, A. E. & Behringer, R. R. Chapter Three - Mammalian uterine morphogenesis and variations. In Gridley, T. & Oxburgh, L. (eds.) *Current Topics in Developmental Biology*, vol. 148 of *Mouse Models of Development and Disease*, 51–77, DOI: 10.1016/bs.ctdb.2021.12.004 (Academic Press, 2022).

17. Casteleyn, C. & Bakker, J. Anatomy of the Rhesus Monkey (Macaca mulatta): The Essentials for the Biomedical Researcher. In *Updates on Veterinary Anatomy and Physiology*, DOI: 10.5772/intechopen.99067 (IntechOpen, 2021).

18. Nakamura, T., Fujiwara, K., Saitou, M. & Tsukiyama, T. Non-human primates as a model for human development. *Stem Cell Reports* **16**, 1093–1103, DOI: 10.1016/j.stemcr.2021.03.021 (2021).

19. Abbas, Y. *et al.* Tissue stiffness at the human maternal–fetal interface. *Hum. Reproduction* **34**, 1999–2008, DOI: 10.1093/humrep/dez139 (2019).

20. Fodera, D. M. *et al.* Material properties of nonpregnant and pregnant human uterine layers. *J. Mech. Behav. Biomed. Mater.* **151**, 106348, DOI: 10.1016/j.jmbbm.2023.106348 (2024).

21. Fang, S. *et al.* Anisotropic Mechanical Properties of the Human Uterus Measured by Spherical Indentation. *Annals Biomed. Eng.* **49**, 1923–1942, DOI: 10.1007/s10439-021-02769-0 (2021).

22. Fang, S. *et al.* Equilibrium Tension and Compression Mechanical Properties of the Human Uterus, DOI: 10.1101/2024.04.25.591208 (2024).

23. Pearsall, G. W. & Roberts, V. L. Passive mechanical properties of uterine muscle (myometrium) tested *in vitro*. *J. Biomech.* **11**, 167–176, DOI: 10.1016/0021-9290(78)90009-X (1978).

24. Conrad, J. T., Johnson, W. L., Kuhn, W. K. & Hunter, C. A. Passive stretch relationships in human uterine muscle. *Am. J. Obstet. Gynecol.* **96**, 1055–1059, DOI: 10.1016/0002-9378(66)90513-8 (1966).

25. Manoogian, S. J., Bisplinghoff, J. A., Kemper, A. R. & Duma, S. M. Dynamic material properties of the pregnant human uterus. *J. Biomech.* **45**, 1724–1727, DOI: 10.1016/j.jbiomech.2012.04.001 (2012).

26. Jayes, F. L. *et al.* Loss of stiffness in collagen-rich uterine fibroids after digestion with purified collagenase Clostridium histolyticum. *Am. J. Obstet. Gynecol.* **215**, 596.e1–596.e8, DOI: 10.1016/j.ajog.2016.05.006 (2016).

27. Omari, E. A., Varghese, T., Kliewer, M. A., Harter, J. & Hartenbach, E. M. Dynamic and Quasi-Static mechanical testing for characterization of the viscoelastic properties of human uterine tissue. *J. biomechanics* **48**, 1730–1736, DOI: 10.1016/j.jbiomech.2015.05.013 (2015).

28. Mak, A. F. The Apparent Viscoelastic Behavior of Articular Cartilage—The Contributions From the Intrinsic Matrix Viscoelasticity and Interstitial Fluid Flows. *J. Biomech. Eng.* **108**, 123–130, DOI: 10.1115/1.3138591 (1986).

bioRxiv preprint doi: https://doi.org/10.1101/2024.11.17.624020; this version posted November 18, 2024. The copyright holder for this preprint (which was not certified by peer review) is the author/funder, who has granted bioRxiv a license to display the preprint in perpetuity. It is made available under aCC-BY-NC 4.0 International license.

29. Suh, J.-K. & DiSilvestro, M. R. Biphasic Poroviscoelastic Behavior of Hydrated Biological Soft Tissue. *J. Appl. Mech.* **66**, 528–535, DOI: 10.1115/1.2791079 (1999).

30. Oftadeh, R., Connizzo, B. K., Nia, H. T., Ortiz, C. & Grodzinsky, A. J. Biological connective tissues exhibit viscoelastic and poroelastic behavior at different frequency regimes: Application to tendon and skin biophysics. *Acta Biomater.* **70**, 249–259, DOI: 10.1016/j.actbio.2018.01.041 (2018).

31. Islam, M. R., Virag, J. & Oyen, M. L. Micromechanical poroelastic and viscoelastic properties of ex-vivo soft tissues. *J. Biomech.* **113**, 110090, DOI: 10.1016/j.jbiomech.2020.110090 (2020).

32. Kirejczyk, S. *et al.* Urogenital Lesions in Nonhuman Primates at Two National Primate Research Centers. *Vet. pathology* **58**, 147–160, DOI: 10.1177/0300985820971752 (2021).

33. Krugner-Higby, L. *et al.* High-risk pregnancy in rhesus monkeys (Macaca mulatta): a case of ectopic, abdominal pregnancy with birth of a live, term infant, and a case of gestational diabetes complicated by pre-eclampsia. *J. Med. Primatol.* **38**, 252–256, DOI: 10.1111/j.1600-0684.2009.00349.x (2009).

34. Bauer, C. & Harrison, T. Retrospective Analysis of the Incidence of Retained Placenta in 3 Large Colonies of NHP. *Comp. Medicine* **66**, 143–149 (2016).

35. Jacobson, H. N. & Windle, W. F. Observations on mating, gestation, birth and postnatal development of Macaca mulatta. *Biol. Neonatorum. Neo-Natal Stud.* **2**, 105–120, DOI: 10.1159/000239792 (1960).

36. Oyen, M. L. & Cook, R. F. A practical guide for analysis of nanoindentation data. *J. Mech. Behav. Biomed. Mater.* **2**, 396–407, DOI: 10.1016/j.jmbbm.2008.10.002 (2009).

37. Shi, L. & Myers, K. A finite porous-viscoelastic model capturing mechanical behavior of human cervix under multi-step spherical indentation. *J. Mech. Behav. Biomed. Mater.* **143**, 105875, DOI: 10.1016/j.jmbbm.2023.105875 (2023).

38. Mow, V. C., Holmes, M. H. & Lai, W. M. Fluid transport and mechanical properties of articular cartilage: a review. *J. Biomech.* **17**, 377–394, DOI: 10.1016/0021-9290(84)90031-9 (1984).

39. Screen, H. R. C., Lee, D. A., Bader, D. L. & Shelton, J. C. An investigation into the effects of the hierarchical structure of tendon fascicles on micromechanical properties. *Proc. Inst. Mech. Eng. Part H: J. Eng. Medicine* **218**, 109–119, DOI: 10.1243/095441104322984004 (2004).

40. Strange, D. G. T. *et al.* Separating poroviscoelastic deformation mechanisms in hydrogels. *Appl. Phys. Lett.* **102**, 031913, DOI: 10.1063/1.4789368 (2013).

41. Islam, M. R. & Oyen, M. L. Load-Relaxation Characteristics of Chemical and Physical Hydrogels as Soft Tissue Mimics. *Exp. Mech.* **61**, 939–949, DOI: 10.1007/s11340-021-00712-x (2021).

42. Zhao, X., Huebsch, N., Mooney, D. J. & Suo, Z. Stress-relaxation behavior in gels with ionic and covalent crosslinks. *J. Appl. Phys.* **107**, 063509, DOI: 10.1063/1.3343265 (2010).

bioRxiv preprint doi: https://doi.org/10.1101/2024.11.17.624020; this version posted November 18, 2024. The copyright holder for this preprint (which was not certified by peer review) is the author/funder, who has granted bioRxiv a license to display the preprint in perpetuity. It is made available under aCC-BY-NC 4.0 International license.

43. Offeddu, G. S., Axpe, E., Harley, B. A. C. & Oyen, M. L. Relationship between permeability and diffusivity in polyethylene glycol hydrogels. *AIP Adv.* **8**, 105006, DOI: 10.1063/1.5036999 (2018).

44. Mow, V. C., Mak, A. F., Lai, W. M., Rosenberg, L. C. & Tang, L. H. Viscoelastic properties of proteoglycan subunits and aggregates in varying solution concentrations. *J. Biomech.* **17**, 325–338, DOI: 10.1016/0021-9290(84)90027-7 (1984).

45. Pajic-Lijakovic, I., Milivojevic, M. & Clark, A. G. Collective Cell Migration on Collagen-I Networks: The Impact of Matrix Viscoelasticity. *Front. Cell Dev. Biol.* **10**, DOI: 10.3389/fcell.2022.901026 (2022).

46. Wang, Q.-M., Mohan, A. C., Oyen, M. L. & Zhao, X.-H. Separating viscoelasticity and poroelasticity of gels with different length and time scales. *Acta Mech. Sinica* **30**, 20–27, DOI: 10.1007/s10409-014-0015-z (2014).

47. Oyen, M. L., Shean, T. A., Strange, D. G. & Galli, M. Size effects in indentation of hydrated biological tissues. *J. Mater. Res.* **27**, 245–255, DOI: 10.1557/jmr.2011.322 (2012).

48. Fernandez, M., Vink, J., Yoshida, K., Wapner, R. & Myers, K. M. Direct Measurement of the Permeability of Human Cervical Tissue. *J. Biomech. Eng.* **135**, DOI: 10.1115/1.4023380 (2013).

49. Scallan, J., Huxley, V. H. & Korthuis, R. J. Pathophysiology of Edema Formation. In *Capillary Fluid Exchange: Regulation, Functions, and Pathology* (Morgan & Claypool Life Sciences, 2010).

50. Negrini, D., Passi, A. & Moriondo, A. The role of proteoglycans in pulmonary edema development. *Intensive Care Medicine* **34**, 610–618, DOI: 10.1007/s00134-007-0962-y (2008).

51. Sheehan, D. C. & Hrapchak, B. B. *Theory and practice of histotechnology* (Mosby, St. Louis, 1980), 2nd edn.

52. Kohn, J. C. & Ebenstein, D. M. Eliminating adhesion errors in nanoindentation of compliant polymers and hydrogels. *J. Mech. Behav. Biomed. Mater.* **20**, 316–326, DOI: 10.1016/j.jmbbm.2013.02.002 (2013).

53. Hu, Y., Zhao, X., Vlassak, J. J. & Suo, Z. Using indentation to characterize the poroelasticity of gels. *Appl. Phys. Lett.* **96**, 121904, DOI: 10.1063/1.3370354 (2010).

54. Mattice, J. M., Lau, A. G., Oyen, M. L. & Kent, R. W. Spherical indentation load-relaxation of soft biological tissues. *J. Mater. Res.* **21**, 2003–2010, DOI: 10.1557/jmr.2006.0243 (2006).

55. Hertz, H. Ueber die Beruhrung fester elastischer Korper. *J. fur die reine und angewandte Math.* **92**, 156–171 (1882).

Acknowledgements

The research was supported in part by the National Science Foundation (NSF) Graduate Research Fellowship (DGE-2036197) to DMF, The Iris Fund, the Eunice Kennedy Shriver National Institute of Child Health Human Development Grant R01HD072077 to TH, IRM, HF, and KM, and the Office Of The Director, NIH Award P51OD011106 to the Wisconsin National Primate Research Center, University of Wisconsin-Madison. We would also like to thank Qi Yan of Columbia University Irving Medical Center for statistics consultation. Figures for this paper were created with BioRender.com, Adobe Illustrator, and GraphPad Prism under registered academic licenses.

bioRxiv preprint doi: https://doi.org/10.1101/2024.11.17.624020; this version posted November 18, 2024. The copyright holder for this preprint (which was not certified by peer review) is the author/funder, who has granted bioRxiv a license to display the preprint in perpetuity. It is made available under aCC-BY-NC 4.0 International license.

Author Contributions Statement

Conceptualization: DMF, KMM

Methodology: DMF, KMM, MLO, XC

Investigation: DMF, EZX, MW

Formal Data Analysis: DMF, EZX

Data Interpretation: DMF, EZX, CADC, MLO, XC, KMM

Resources: SF, TH, IRM, HF, KMM, JYV

Writing, Original Draft: DMF

Writing, Review and Editing: DMF, EZX, CADC, XC, MLO, IRM, JYV, TH, KMM

Visualization: DMF

Supervision: KMM

Funding Acquisition: TH, IRM, HF, KMM

Competing Interests Statement

The authors declare that they have no competing interests.

Data and materials availability

All original data will be made available on Columbia University's Academic Commons; a link will be provided upon journal acceptance. Codes used for data analysis are available upon request.

bioRxiv preprint doi: https://doi.org/10.1101/2024.11.17.624020; this version posted November 18, 2024. The copyright holder for this preprint (which was not certified by peer review) is the author/funder, who has granted bioRxiv a license to display the preprint in perpetuity. It is made available under aCC-BY-NC 4.0 International license.

480 # Figures & Tables

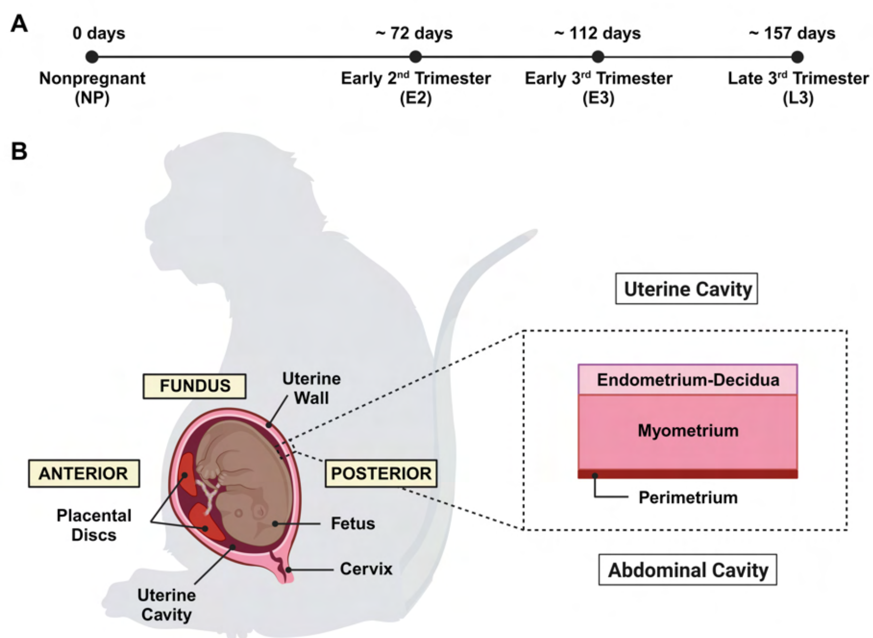

Figure 1. Pregnant Rhesus Macaque Anatomy. **(A)** Timeline of Rhesus macaque pregnancy. **(B)** Representative illustration of pregnant Rhesus Macaque anatomy in the sagittal plane. Relevant reproductive structures and anatomic regions (anterior, fundus, and posterior) are labeled, including a detailed schematic of the uterine wall containing all three uterine layers (endometrium-decidua, myometrium, perimetrium).

Animal ID	Age (yrs)	Gestational Age (days)	Gravidity	Placenta Disc Locations (Primary & Secondary)	Past Obstetric History
NP-1	4.1	N/A	0	N/A	None
NP-2	15.2	N/A	5	N/A	VDx4, CSx1
NP-3	11.8	N/A	5	N/A	VDx5
E2-1	15.2	72	7	Unknown	VDx4, CSx3
E2-2	8.9	71	3	Posterior Lateral & Anterior Lateral	VDx2, CSx1
E2-3	11	73	1	Anterior & Posterior	VDx1
E3-1	8	110	3	Anterior & Posterior	VDx3
E3-2	18	112	3	Fundo-Anterior & Posterior	VDx5, CSx3
E3-3	17.8	119	4	Anterior & Posterior	VDx1, CSx3
L3-1	16	161	8	Anterior Lateral & Posterior Lateral	VDx5, CSx3
L3-2	9.7	158	4	Anterior & Posterior-Fundus	CSx4
L3-3	18.4	152	2	Anterior Lateral & Posterior Lateral	VDx1, CSx1
L3-4	12	157	5	Anterior & Posterior	VDx3, CSx2
L3-5	14.2	154	4	Unknown	VDx2, CSx2

Table 1. Detailed Summary of Individual Nonhuman Primate Characteristics. VD ≡ Vaginal delivery, CS ≡ Cesarean section.

bioRxiv preprint doi: https://doi.org/10.1101/2024.11.17.624020; this version posted November 18, 2024. The copyright holder for this preprint (which was not certified by peer review) is the author/funder, who has granted bioRxiv a license to display the preprint in perpetuity. It is made available under aCC-BY-NC 4.0 International license.

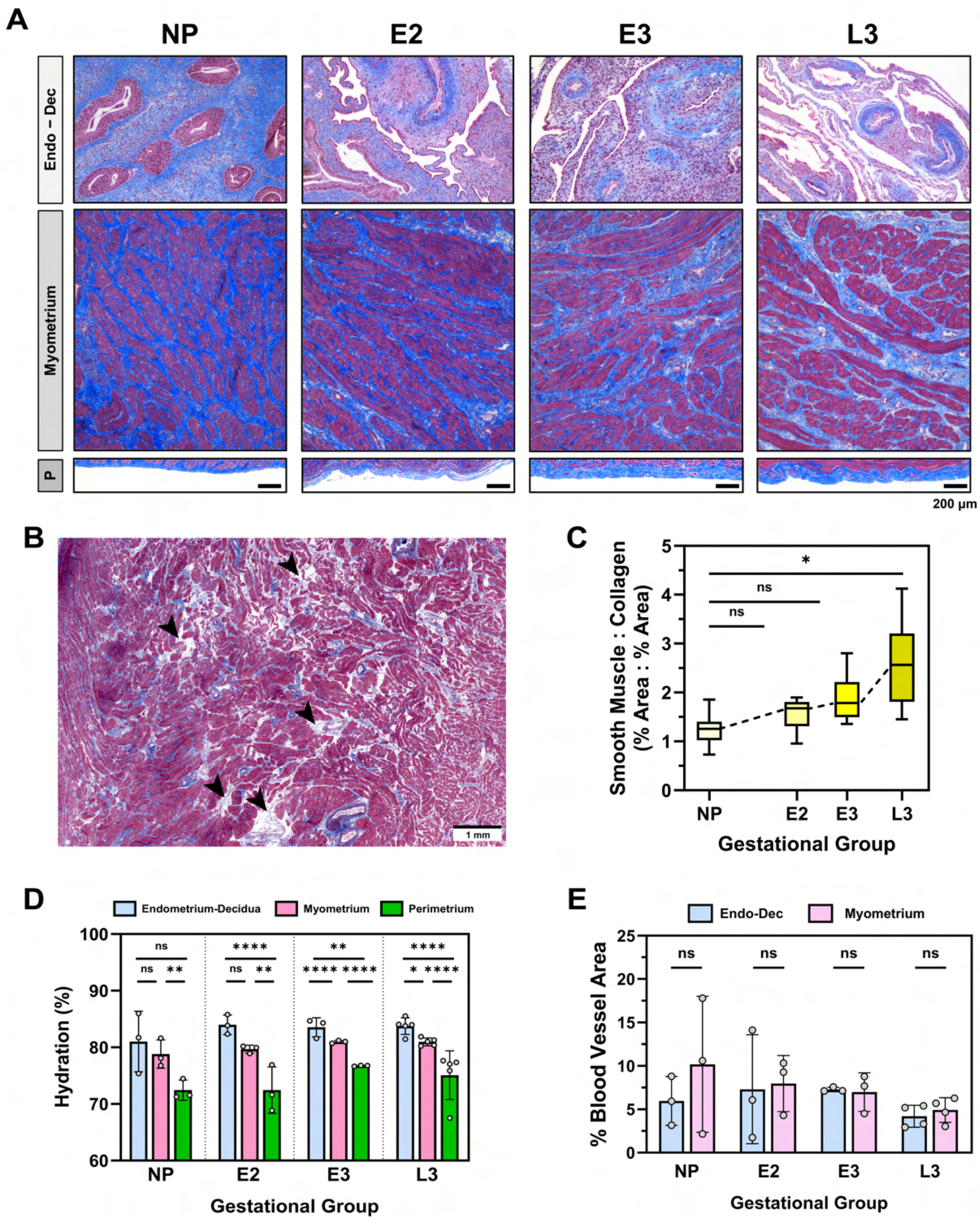

Figure 2. **(A)** Histology of NHP uterine layers [endometrium-decidua (Endo-Dec), myometrium, and perimetrium (P)] across gestation. Tissues are stained with Masson's Trichrome (blue = collagen; red = smooth muscle, cytoplasm; black = nuclei). Note that the relative lengths of the tissue layer figure panels do not reflect actual layer proportions. **(B)** Representative image of focal edema in the L3 myometrium. **(C)** Ratio of smooth muscle to collagen content in the myometrium across gestation. **(D)** Tissue hydration of all uterine layers across gestation. **(E)** Proportion of blood vessel area in the endometrium-decidua and myometrium across gestation.

bioRxiv preprint doi: https://doi.org/10.1101/2024.11.17.624020; this version posted November 18, 2024. The copyright holder for this preprint (which was not certified by peer review) is the author/funder, who has granted bioRxiv a license to display the preprint in perpetuity. It is made available under aCC-BY-NC 4.0 International license.

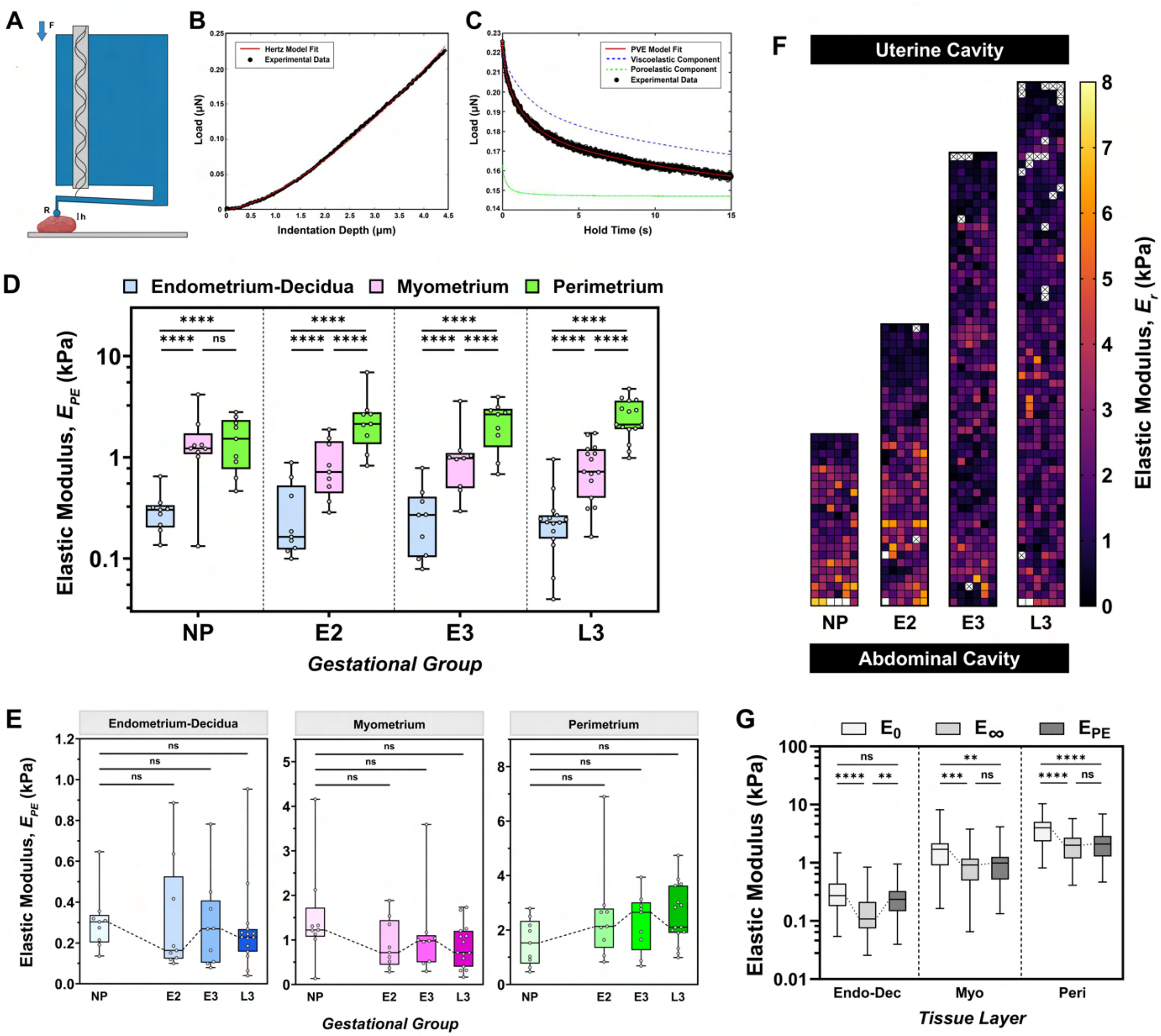

Figure 3. **(A)** Schematic of the Piuma Nanoindentor (Adapted from Optics11 Life). A spherical probe with radius (R) is attached at the end of a cantilever and indented into the sample at a fixed depth (h), recording load (F) over time. **(B)** Representative load vs indentation data fitted with the Hertzian contact model. **(C)** Representative load vs time data fitted with the PVE model. **(D-E)** Elastic modulus (E_{PE}) of the NHP uterus **(D)** across tissue layers and **(E)** across gestation. Each point represents the median value of all indentation points measured for a single sample. **(F)** Spatial variation in local elastic modulus/stiffness (E_r) values across the uterine walls of NP, E2, E3, and L3 subjects. Measurements were taken at every 200 μm across the length of the tissue. Points removed due to exclusion criteria are represented by [X]. White squares indicate data points outside the bounds of the y-axis. **(G)** Comparison of viscoelastic (E_0, E_∞) and poroelastic (E_{PE}) elastic modulus parameters for each tissue layer with data being pooled from all gestational groups.

bioRxiv preprint doi: https://doi.org/10.1101/2024.11.17.624020; this version posted November 18, 2024. The copyright holder for this preprint (which was not certified by peer review) is the author/funder, who has granted bioRxiv a license to display the preprint in perpetuity. It is made available under aCC-BY-NC 4.0 International license.

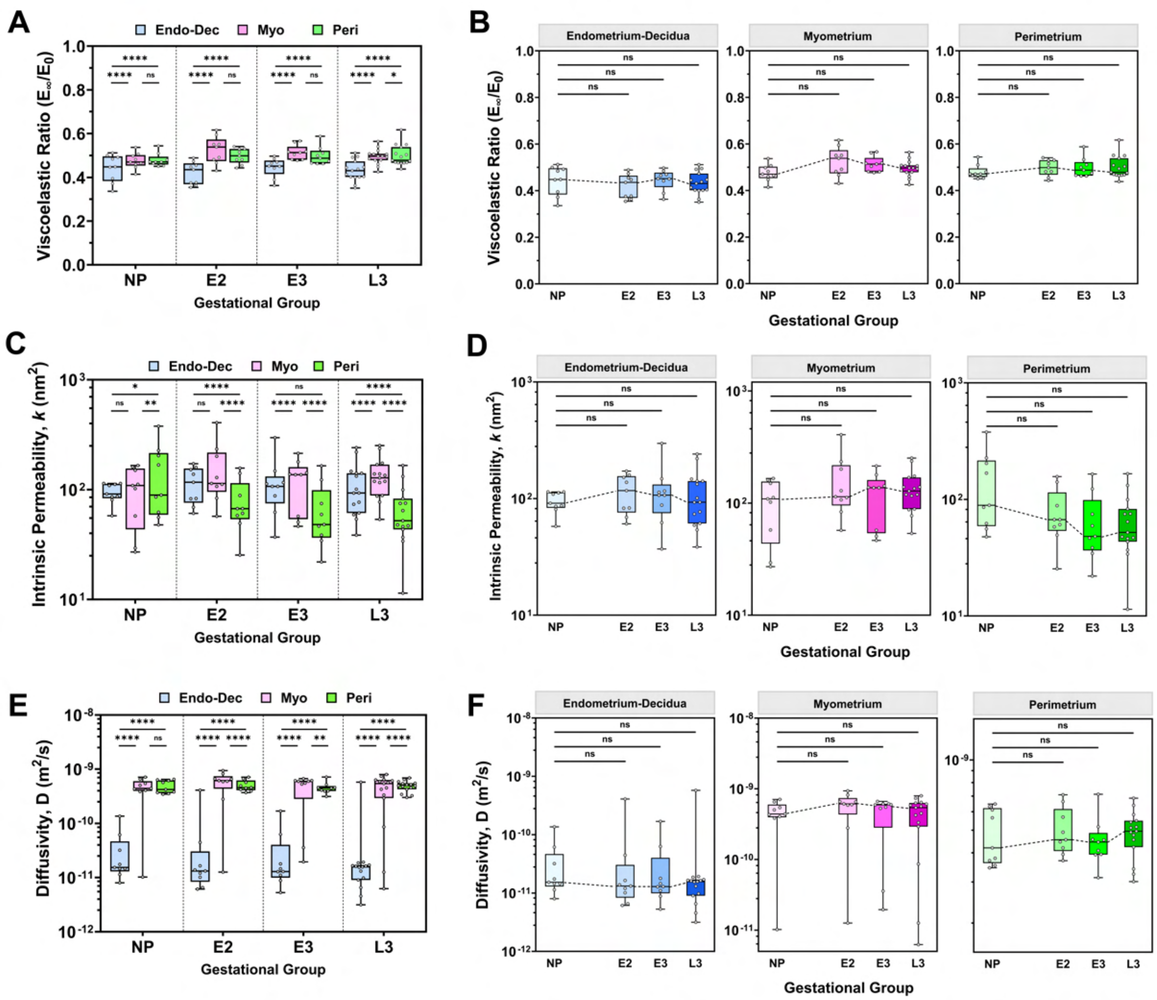

Figure 4. Viscoelastic Ratio **(A, B)**, Intrinsic Permeability **(C, D)** and Diffusivity **(E, F)** of NHP Uterus Across Tissue Layers **(A, C, E)** and Across Gestation **(B, D, F)**. Each point represents the median value of all indentation points measured for a single sample.

bioRxiv preprint doi: https://doi.org/10.1101/2024.11.17.624020; this version posted November 18, 2024. The copyright holder for this preprint (which was not certified by peer review) is the author/funder, who has granted bioRxiv a license to display the preprint in perpetuity. It is made available under aCC-BY-NC 4.0 International license.

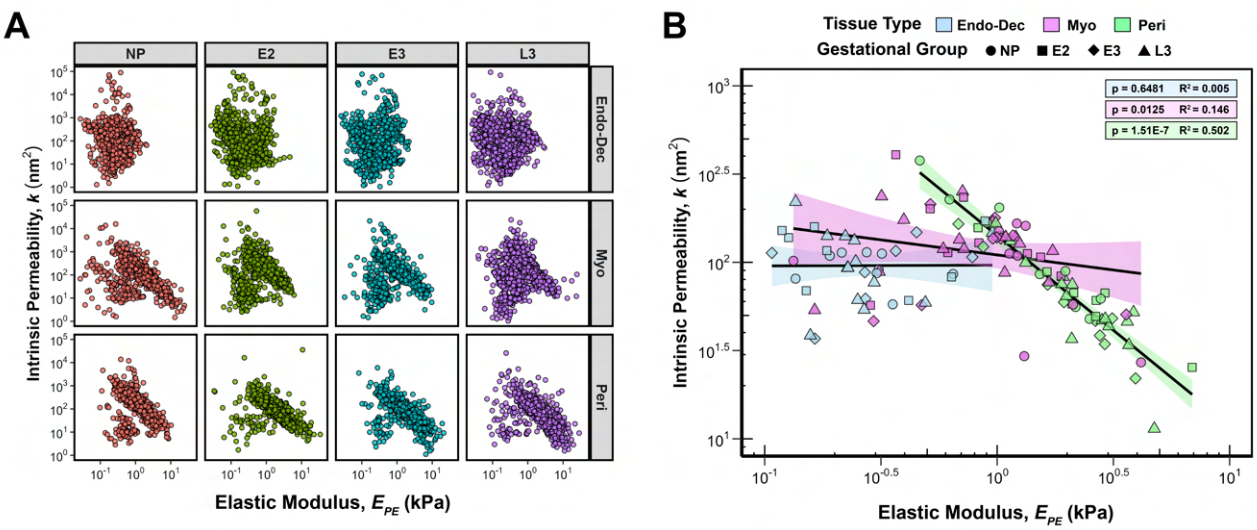

Figure 5. Correlation of elastic modulus (E_{PE}) and intrinsic permeability (k) parameters for **(A)** all data points, separated by tissue layer and gestational group, and **(B)** median values for each sample, separated by tissue layer. Linear regression analysis was performed for each tissue layer with data being pooled across all gestational groups. R^2 and p values are noted; shaded regions indicate the 95% confidence interval.

bioRxiv preprint doi: https://doi.org/10.1101/2024.11.17.624020; this version posted November 18, 2024. The copyright holder for this preprint (which was not certified by peer review) is the author/funder, who has granted bioRxiv a license to display the preprint in perpetuity. It is made available under aCC-BY-NC 4.0 International license.

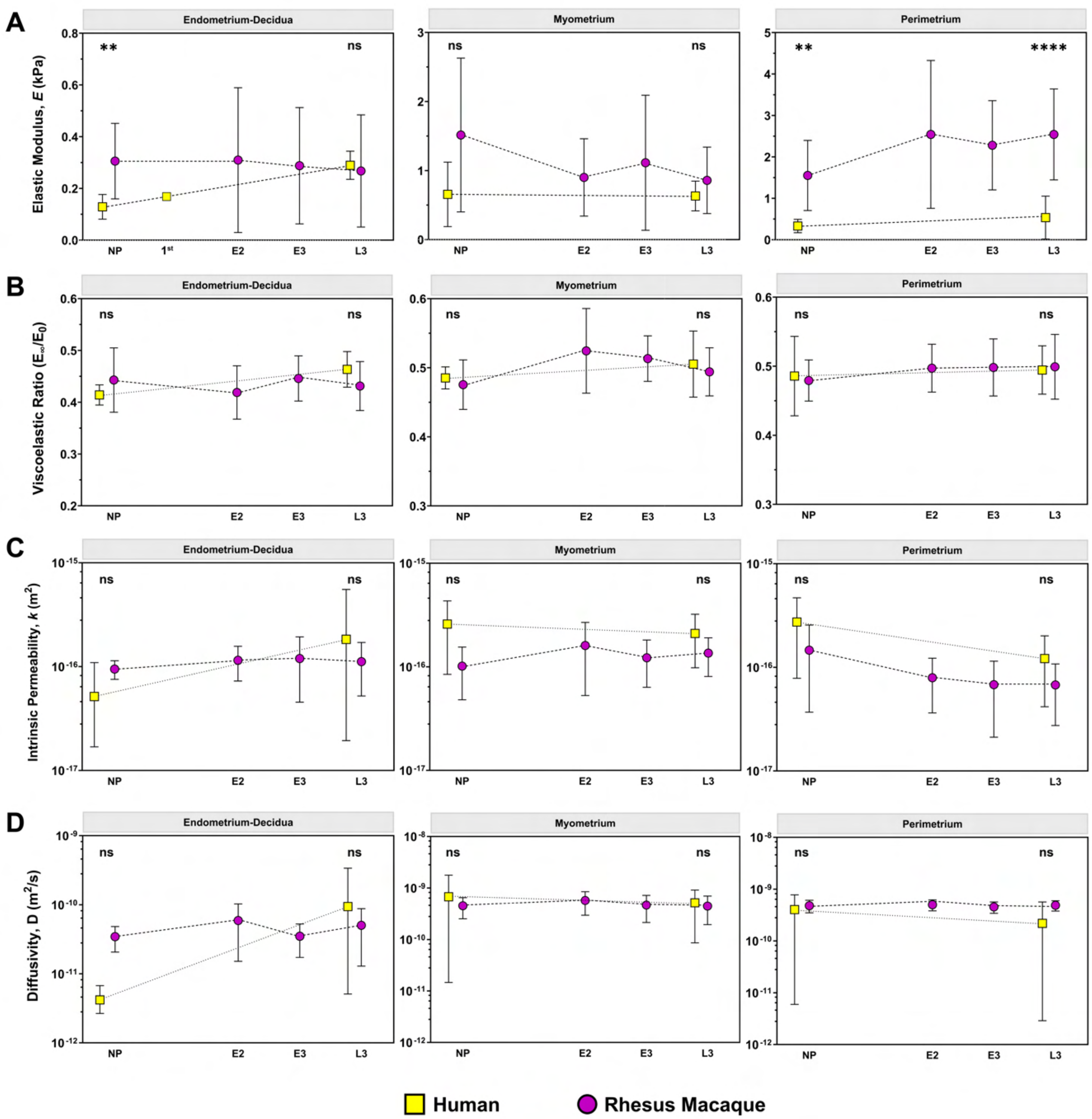

Figure 6. Comparison of Rhesus Macaque and Human Micromechanical Uterine Properties Across Gestation. Human data was taken from Fodera et al. (2024) for nonpregnant and late third-trimester (PG-CS) states and Abbas et al. (2019) for the first-trimester time point. Statistical significance between NHP and Human data was computed for NP and L3 groups.

bioRxiv preprint doi: https://doi.org/10.1101/2024.11.17.624020; this version posted November 18, 2024. The copyright holder for this preprint (which was not certified by peer review) is the author/funder, who has granted bioRxiv a license to display the preprint in perpetuity. It is made available under aCC-BY-NC 4.0 International license.

Supplemental Information

Supplemental Figures & Tables

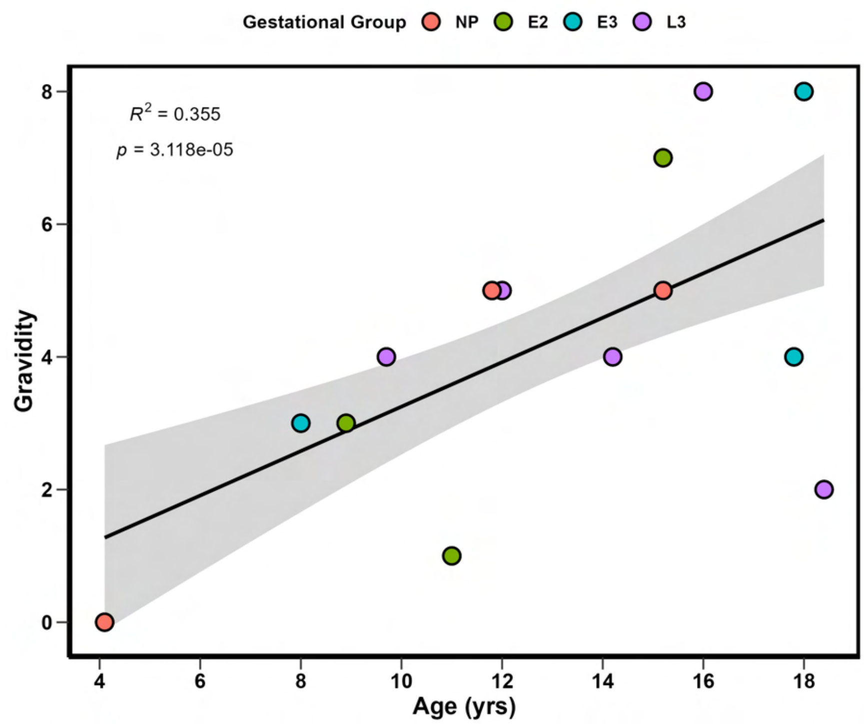

Figure S1. Correlation between age and gravidity for animal subjects studied in this cohort. R^2 and p values are noted.

Animal ID	Estimated Menstrual Cycle Stage	Additional Pathological Findings
NP-1	Proliferative	Nodular and disorganized myometrium
NP-2	Unknown – Basalis tissue only	Fibrous basalis tissue; Fibrosis of serosa
NP-3	Late Proliferative / Early Secretory	Adenomyosis
E2-1	N/A. Decidua Parietalis	None
E2-2	N/A. Decidua Parietalis	None
E2-3	N/A. Decidua Parietalis	None
E3-1	N/A. Decidua Parietalis	None
E3-2	N/A. Decidua Parietalis	Endosalpingiosis; Notable fibrotic scar tissue that extends vertically from serosa to decidua – indicative of a previous C-section incision
E3-3	N/A. Decidua Parietalis	Focal thickening of serosa
L3-1	N/A. Decidua Parietalis	None
L3-2	N/A. Decidua Parietalis	None
L3-3	N/A. Decidua Parietalis	None
L3-4	N/A. Decidua Parietalis	None
L3-5	N/A. Decidua Parietalis	None

Table S1. Summary of histological findings for all NHP subjects with estimated menstrual cycle stage for NP individuals.

bioRxiv preprint doi: https://doi.org/10.1101/2024.11.17.624020; this version posted November 18, 2024. The copyright holder for this preprint (which was not certified by peer review) is the author/funder, who has granted bioRxiv a license to display the preprint in perpetuity. It is made available under aCC-BY-NC 4.0 International license.

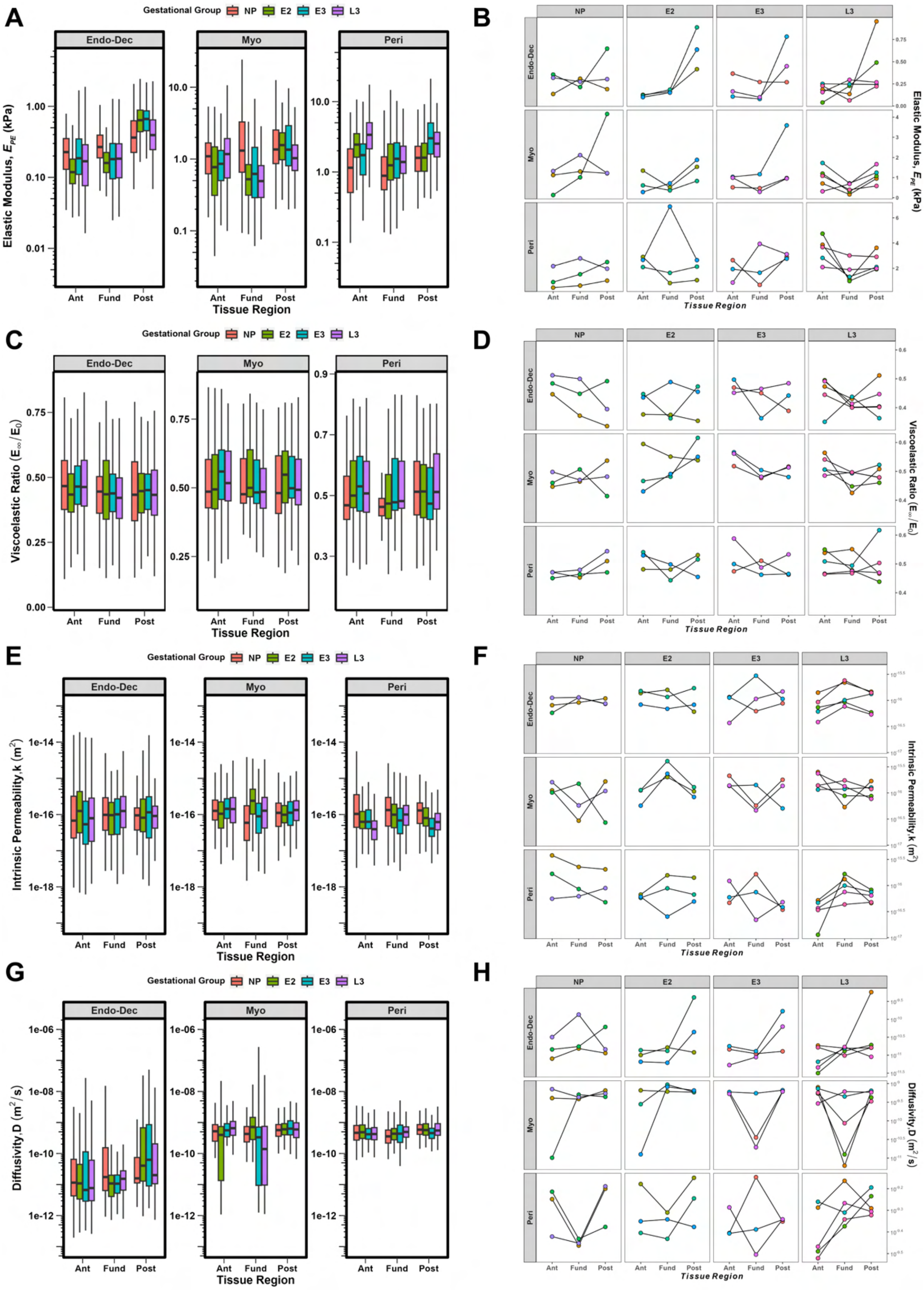

Figure S2. **Variations in Material Properties Across Anatomic Regions (Anterior, Fundus, Posterior)**. Elastic modulus (A,B), viscoelastic ratio (C,D), intrinsic permeability (E,F), and diffusivity (G,H). All data for a given tissue layer, gestational group and anatomic region are shown as box and whisker plots (left column). The right column depicts matched values for each tissue layer and gestational group for a given animal across the three anatomic regions. Each point represents the median value of all indentation points measured for a single sample.

bioRxiv preprint doi: https://doi.org/10.1101/2024.11.17.624020; this version posted November 18, 2024. The copyright holder for this preprint (which was not certified by peer review) is the author/funder, who has granted bioRxiv a license to display the preprint in perpetuity. It is made available under aCC-BY-NC 4.0 International license.

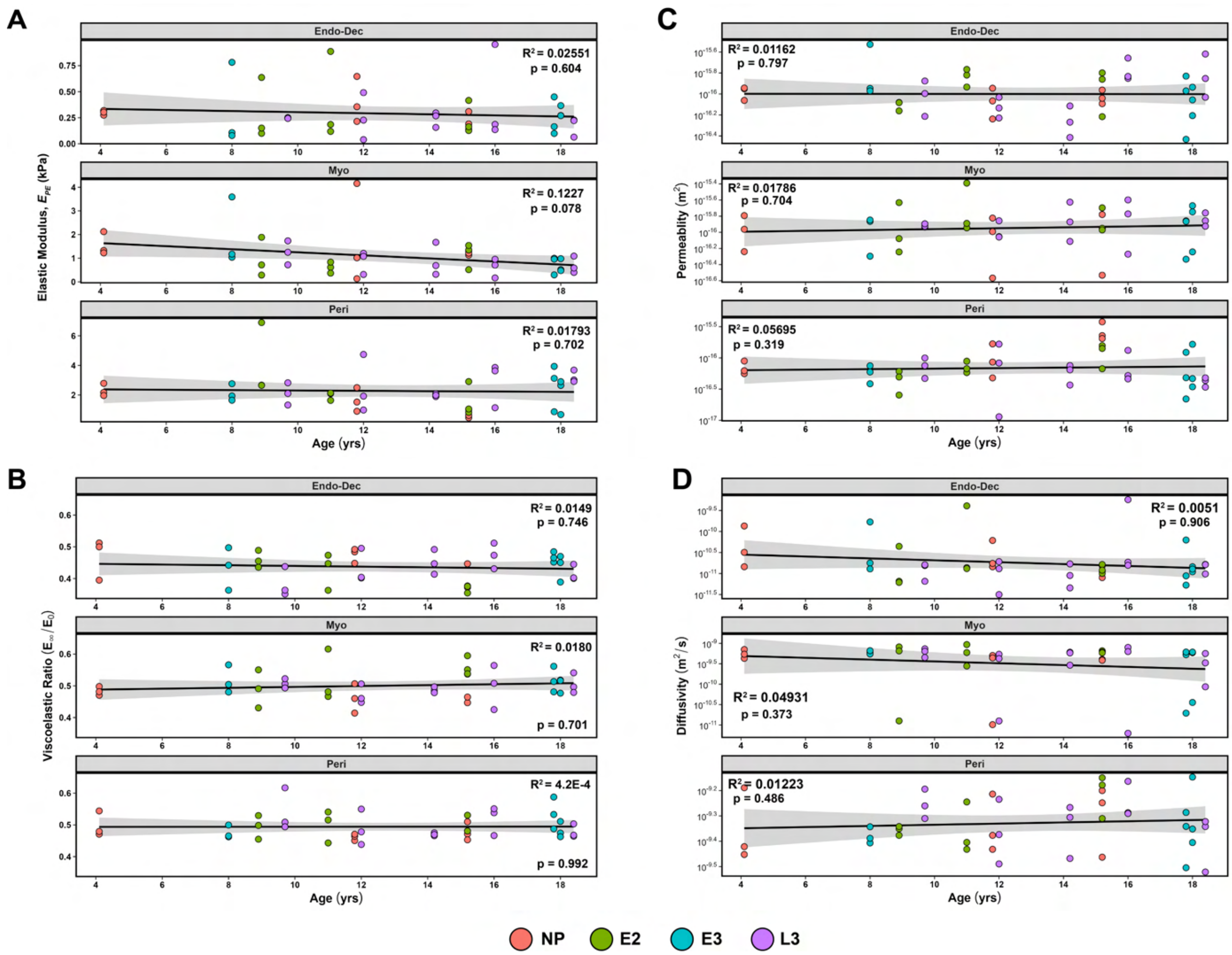

Figure S3. Correlation of Uterine Layer Mechanical Parameters with Animal Age. Each point represents the median value of all indentation points measured for a single sample. The R^2 and p values for each correlation are noted. Standard deviations are indicated by the shaded grey areas.

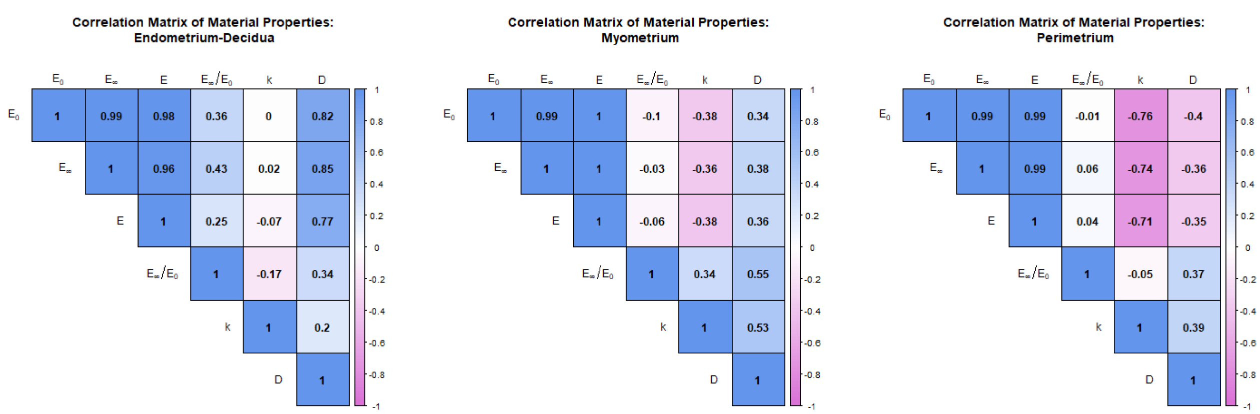

Figure S4. Inter-correlation of Material Parameters by Uterine Tissue Layer. Values close to -1, shown in pink, indicate a strong negative correlation between the two parameters, while values close to 1, shown in blue, indicate a strong positive correlation.